Vol.7 No.3 July 2024

Multimedia Research

Received 20 May, Revised 17 June, Accepted 14 July

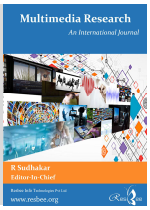

Skin Disease Detection with Social Crow Search Optimization Algorithm- Based Deep Recurrent Neural Network

Phani Kulkarni

University of Missouri Kansas
Kulkarniphani@gmail.com

Abstract: Skin diseases are more common than other diseases. Skin diseases may be caused by fungal infections, bacteria, allergies, viruses, etc. The advancement of lasers and photonics-based medical technology has made it possible to diagnose skin diseases much more quickly and accurately. However, the cost of such a diagnosis is still limited and very expensive. Hence, this paper introduces an accurate and effective skin disease detection method, named the Social Crow Search (SCS) algorithm proposed in this research work. Initially, the pre-processing is done for the input image to eliminate the noise and artifacts present in the image. Then, the pre-processed image is fed to the segmentation step where the segmentation is performed using Black Hole Entropic Fuzzy Clustering (BHEFC). Consequently, the segmented results are subjected to the feature extraction step in which the features, like Convolutional Neural Network (CNN) features, Grey Level Co-occurrence Matrix (GLCM) features and the convolution-based Local Directional Pattern (LDP) features are extracted to increase the accuracy. Finally, the skin disease is detected using SCS-based Deep RNN. The optimal solution is revealed through the fitness measure, which in turn accepts the minimal error value as the optimal solution. The proposed SCS-based Deep RNN attained significantly better performance in accurately detecting the disease. The proposed model achieves the maximal accuracy of 93.54%, maximal sensitivity of 93.56%, and maximal specificity of 93.45%, respectively to training data percentage.

Keywords: Skin Disease Detection, Deep Recurrent Neural Network, Black Hole Entropic Fuzzy Clustering, Social Sky Driver, Crow Search Algorithm.

Nomenclature

Abbreviation	Expansion
BCC	Basal Cell Carcinoma
SCC	Squamous Cell Carcinoma
AK	Actinic Keratosis
UVR	UltraViolet Radiation
OCT	Optical Coherence Tomography
PDT	Photodynamic Therapy
AFL	Ablative Fractional Laser
OTR	Organ Transplant Recipients
Deep RNN	Deep Recurrent Neural Network
SSD	Social Sky Driver
CSA	Crow Search Algorithm
BHE	Black Hole Entropy
MAP	Maximum-a-Posteriori
ReLU	Rectified Linear Unit
TNR	True Negative Rate

1. Introduction

Skin is composed of three primary layers: epidermis, dermis, and hypodermis (subcutaneous adipose layer). The epidermis is divided into three layers: Malpighian (basal and squamous) layer, granular layer, and cornified layer. Lesions are found on sites of sun-exposed skin such as the face, balding scalp, chest, forearms, and back of the hand [7]. Skin cancers are by far the most prevalent neoplasia observed in OTR [7]. The occurrence of skin cancer in OTR varies depending on the grafted organ; the composition, intensity, and duration of immunosuppressive treatments; as well as UVR exposure and genetic factors [7]. Non-melanoma skin cancer, including BCC and SCC of the skin, are the most common malignancies in humans. BCC and SCC share essential characteristics. They both are derived from epidermal keratinocytes and are

https://doi.org/10.46253/j.mr.v7i3.a2

associated with ultraviolet light exposure, fair skin, and immunosuppression. Nevertheless, SCC has a greater tendency to metastasize and frequently arises from precursor lesions, such as AK, while BCC only very rarely metastasizes and arises directly from healthy skin [8]. SCC is a malignant tumor characterized by keratinocytes arising in the epidermis, with histological evidence of dermal invasion. It is the second most common type of skin cancer, and its incidence has been increasing steadily. It predominantly occurs in the elderly and its incidence has been rising with the increasing elderly population [5] [12].

More and more studies have demonstrated that the tumor microenvironment plays a vital role in the progression of SCC. The tumor microenvironment is closely related to tumorigenesis, tumor progression, and metastasis [5]. Numerous genetic alterations have been described in SCC subtypes, although the molecular mechanisms contributing to tumor initiation and progression are still being studied [3]. Although most cutaneous SCCs are diagnosed early and successfully treated by surgical excision, in a small proportion of cases, especially if neglected, they may show uncontrollable growth and substantial disfigurement and may possess features associated with a high likelihood of recurrence, metastasis, and death. Such cases involving giant cutaneous SCCs (maximum diameter >5 cm) can be very difficult to treat and can present with recurrence and/or metastasis despite aggressive excision [3]. AK are lesions formed from the proliferation of transformed neoplastic keratinocytes in the epidermis, resulting from cumulative UVR from sun exposure [7] [9] [10]. The presence of AKs is a clinical sign of photo carcinogenesis. These precancerous lesions can lead to SCC [6]. A frequent first step in the pathogenesis of AKs is the UV-induced mutation of p53, which is followed by other gene mutations and epigenetic alterations, increased proliferation, and decreased elimination of damaged keratinocytes, leading to AKs or even SCC. Furthermore, UV-induced inflammation (COX-2) and immunosuppression (increased number of Foxp3+ T reg cells, isomerization of trans-urocanic acid to cis-urocanic acid) also contribute to photo carcinogenesis. Multiple presentations within one area assign field cancerization [6]. AKs may present on a patient as visible lesions, of which 5–10% have the potential to transform into SCC [7] [11]

Following the increasing demand for non-invasive treatments and swift diagnostic procedures, many skin imaging techniques have been developed. One of the promising tools is OCT. It is based on interferometry using infrared light. In ophthalmology, the technique is used as a routine procedure for high-resolution imaging of the retina and cornea. In dermatology, OCT was introduced in 1997 and has since then been studied in a range of dermatological diseases and structures. OCT provides real-time high-resolution cross-sectional2D and 3D images measuring a skin area of up to 6 × 6 mm with a penetration depth of 1–2 mm [2]. PDT is a field treatment modality. PDT shows very good therapeutic efficacy and excellent cosmetic outcomes [6]. However, higher complete clearance rates are reported if PDT follows Er:YAG (erbium:yttrium-aluminium-garnet) or CO2 AFL pretreatment. The reason might be the higher penetration of photosensitizer through the ablative laser-induced microscopic holes [6]. In OTR as a consequence of long-term immunosuppressive therapy, the risk of developing cutaneous SCC is much higher, with an almost 250-fold increase compared with immune-competent individuals [7] [13] [14].

The purpose of the research is to present a skin disease detection strategy for which the proposed SCS-based Deep RNN is employed. Here, the BHEFC is employed for obtaining the segments from which the skin disease regions are easily identified. In addition, the features, like CNN features, GLCM features, and the LDP features are extracted for determining the skin diseases. In addition, Deep RNN is employed for detecting skin disease using the features. Finally, the Deep RNN is trained by the proposed SCS in such a way that the model parameters are learned optimally. SCS is the proposed algorithm, which is developed through the inheritance of the high global convergence property in the CSA algorithm. Hence, the proposed SCS-based Deep RNN renders effective accuracy while facilitating skin disease detection. The training of Deep RNN is performed using the proposed SCS algorithm which is the integration of SSD and CSA algorithms.

The major contribution of the paper is:

Proposed SCS-based Deep RNN for skin disease detection: The skin disease detection model is achieved using the proposed SCS-based Deep RNN classifier. The characteristic features of SCS yield the classifier optimally to achieve the best detection result through the optimal fitness value. The fitness measure is evaluated based on the position of the crow, which in turn reflects the accuracy and robustness of the detection measure. In addition, the convolution-based LDP is introduced, which is the combination of convolution operation and LDP to extract the features for better skin disease detection.

2. Motivation

This section illustrates the review of previous techniques along with demerits, which highlight the challenges of the work, serving as the motivation for proposing a novel skin disease detection scheme.

2.1 Literature Survey

Several methods related to skin disease detection are described and analyzed as follows**:** Noroozi, N. and Zakerolhosseini, A. [1] developed an automated approach for Cutaneous SCCdiagnosis from AK. Once the segmentation and cornified layer removal, the axis of the epidermis was specified based on the paths in the granular and skeleton layer was eliminated through the connected components. At last, the diagnosis was carried out using the classification result of the extracted intensity profiles from the lines perpendicular to the epidermis axis. The method failed to perform automated diagnosis of non-pigmented skin lesions.

Olsen, J *et al.* [2] developed an approach for diagnosing accuracy of the optical tomography in basal cell carcinoma and AK. This approach was utilized to differentiate lesions from normal skin. The method diagnoses the BCC lesions effectively, but the accuracy was not found better.

In 2022, Allugunti, V.R., [3] have presented DL and CNN techniques to identify melanoma in the early stages of skin diseases. Initially, input data were collected and an image processing technique was applied to increase the quality of the image. Then CNN was applied to classify the lesion as malignant, superficial spreading, and nodular melanoma. Finally, the data was evaluated and compared to find the effectiveness of the data. This method was reliable in the diagnosis of melanoma at an early stage. However, the dataset of picture data was not readily available in all clinical settings.

Sakthivel, P *et al.* [4] modelled Aggressive multimodality treatment to detect the unusual neoplasm more accurately. However, the patient's long-term prognosis remains unknown and requires prolonged surveillance.

In 2023, Wei *et al.* [5] rendered the CNN method of the classification of skin disease. Initially, the CNN model was used for training and testing basic private datasets dominated by acne-like skin disease. Using classification performance, the best-performing models were selected. Furthermore, pre-training, data augmentation, and parameter fine-tuning were used to upgrade the classification performance of the model. The attention module was additionally introduced to strengthen the feature extraction capacity of the model. Finally, the model was evaluated with the existing model to compare its performance. The result achieved was good in both private and public datasets. However, only limited datasets were used for evaluation.

In 2023, Roy *et al.* [6] adopted an augmentation method to detect Melanoma in the skin. Initially, datasets were collected through Kaggle. The data augmentation technique was applied to select the images in the proper orientation. Then the data was trained through the ViT model and evaluated to find its accuracy.

Joly, F *et al.* [7] presented Photodynamic therapy for correcting the abnormal cancer gene expression in the actinic keratosis lesions and induces the remodeling effect of photodamaged skin. However, the method failed to analyze the protein level.

In 2023, Abd El-Fattah *et al.* [8] used an Enhanced Deep Super-Resolution Generative Adversarial Network (EDSR-GAN) to obtain High-resolution skin disease images. Initially, using EDSR-GAN high-resolution image was obtained. From that, a new design of loss function was created. Furthermore, the HR images were evaluated in various metrics and compared with other datasets to obtain accurate results. This method obtained accurate results in color, texture, and recognition.

2.2 Challenges

The challenges faced by the existing method are illustrated as follows:

- The main challenge with the carcinoma strategies is nuclei segmentation, as all of the features used in the diagnosis and grading stage depend on the accuracy of this task [1].
- The diagnostic accuracy of OCT in NMSC was less accurate than the clinical diagnosis, with difficulties in differentiating BCC from actinic keratosis (AK). This may suggest that the diagnostic features were too subtle and difficult to recognize in the OCT images [2].
- Head and neck teratomas represent a considerable diagnostic challenge due to a lack of awareness among pathologists and clinicians, and the presence of varied tissue components, only a few of which are represented on small biopsies, leading to multiple discrepant diagnoses [4].
- There is a higher risk of accumulating DNA mutations during the continuous division process of chronically UVR-exposed basal keratinocytes than in non-sun-exposed skin [7].
- It is characteristic that the different biological principles, which may influence the outcome of radiotherapy in head and neck cancer to a large extent, have been subjected to numerous and frequently large randomized trials and, therefore, there exists abundant information to evaluate the evidence for such therapeutic interventions. Moreover, hypoxic modification is an issue to be considered in modern radiotherapy [10].

3. Proposed Social Crow Search-Based Deep Recurrent Neural Network For Skin Disease Detection

In this section, the proposed SCS-enabled Deep RNN for skin disease detection. Initially, the input image is given to the pre-processing phase, where the external artifacts and the noise present in the image are removed. The pre-processed image is further fed to the segmentation phase, where images are effectively segmented using BHEFC. The segmented results ensure the effectiveness of the image for further processing. The segmented result is then subjected to the feature extraction phase, where the features, such as CNN features, GLCM features, and the convolution-based LDP features are effectively extracted, which in turn increases the accuracy of classification. Finally, the features extracted from the extraction module are given to the classification phase, where the skin disease classification is carried out using the Deep RNN classifier. The weights in the Deep RNN will be trained using the proposed SCS optimization algorithm, which is the integration of CSA [16], and SSD optimization algorithm [15], respectively. Fig. 1 represents the schematic diagram of the developed SCS-enabled Deep RNN.

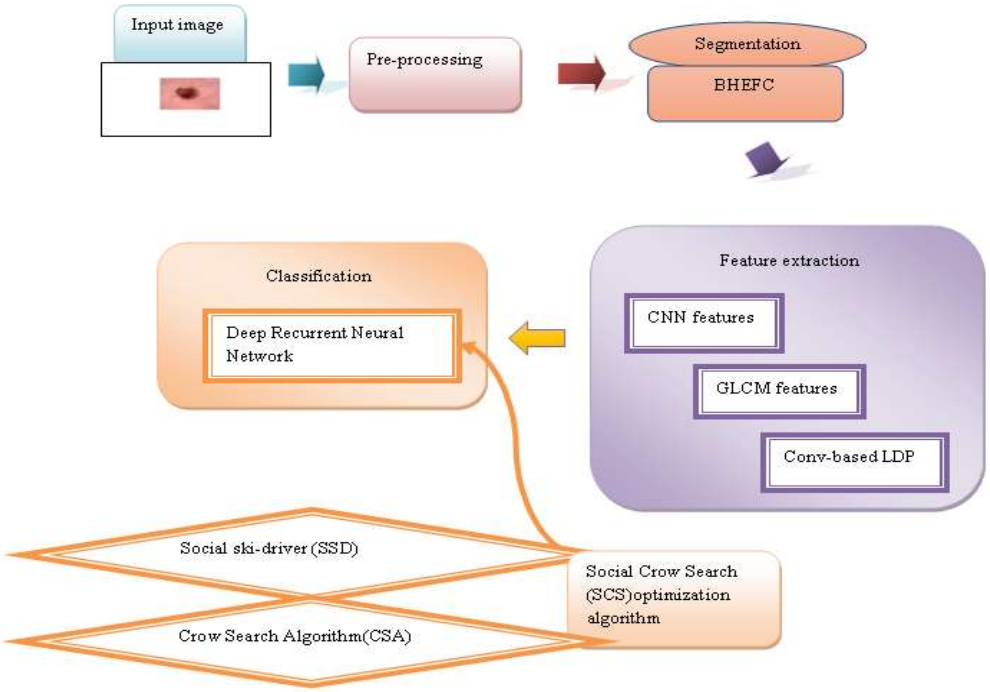

Fig. 1. *Schematic view of the proposed SCS-based Deep RNN*

3.1 Read the Input Image

The image is initially selected randomly to perform the detection mechanism among the number of images from the dataset. Let us consider the database B with h a number of images represented as

$$B = \{B_1, B_2, ..., B_u, ..., B_s\} \tag{1}$$

where, the image is denoted as B, the total number of images is represented as B_s, and B_u signifies the u^{th} image, which is selected as the input image for processing the detection mechanism.

3.2 Pre-Processing

The initial step of skin disease detection is pre-processing. The input image B_u is subjected to the pre-processing module to improve the contrast of the image to make it appropriate for further processing. where the external artifacts and the noise present in the image will be removed. Here, the robustness and the accuracy of the imageare improved by removing the uninterested regions, and the pre-processed image is denoted as, G_q .

3.3 Black Hole Entropic Fuzzy Clustering for Segmentation

Segmentation is defined as the process of partitioning the preprocessed image into several segments, like image or pixel objects. The pre-processed image G_q is subjected to the segmentation module from which

the segmentation is performed based on BHEFC [18]. The BHEFC is utilized for generating the samples using the fuzzy membership function. In addition, the BHEFC performs the segmentation process by considering fuzzy clustering, the Bayesian inference model, and BHE-enabled information. However, the BHEFC is designed by combining the BHE and fuzzy clustering, which effectively and accurately characterizes the clustering behavior based on MAP. The BHEFC is modeled based on fuzzy c-means clustering and the principle of Lagrangian optimization, and is represented as,

$$\tilde{Q}\left(G_q, d_q \mid R\right) = Q\left(G_q, \mid d_q, R\right).Q\left(d_q\right).\gamma.\prod_{n=1}^{P}\exp\left\{-\frac{1}{2}d_q^b\left\|G_q - X_n\right\|^2\right\}d_q^{-b} \tag{2}$$

$$Y_p = \min\left\{1, \frac{\tilde{Q}\left(G_q, d_q^+ \mid R\right)}{\tilde{Q}\left(G_q, d_q \mid R\right)}\right\} \tag{3}$$

$$Q\left(M, X_q \mid S\right) = Q\left(M \mid V, X_q\right)Q\left(X_q\right).\gamma.\exp\left\{-\frac{1}{2}\sum_{q=1}^{\kappa}d_q^b\left\|G_q - X_n\right\|^2\right\}\exp\left\{-\frac{1}{2}\left(\eta + \beta\sum_{q=1}^{\kappa}\ln\left\|G_q - X_q\right\|^2\right)\right\} \tag{4}$$

$$Y_Z = \min\left\{1, \frac{Q\left(M, X_n^+ \mid S\right)}{P\left(N, X_n \mid S\right)}\right\} \tag{5}$$

$$\begin{aligned} Q(M,S,R) = Q(M \mid S,R)\tilde{Q}(S \mid R).\tilde{Q}(R)\gamma.\exp\left\{-\frac{1}{2}\sum_{q=1}^{\kappa}\sum_{n=1}^{P}d_q^b\left\|G_q - X_n\right\|^2\right\}\times\left(\prod_{q=1}^{\kappa}\prod_{n=1}^{P}d_q^{-b}\right)\times \\ \exp\left\{-\frac{1}{2}\left(\eta + \beta\sum_{q=1}^{\kappa}\sum_{n=1}^{P}\ln\left\|G_q - X_n\right\|^2\right)\right\} \end{aligned} \tag{6}$$

where, the terms γ and β is denoted as vectors, which are fixed to two to simplify the segmentation process. G_q indicates the pre-processed image, the term d_q refers to the fuzzy membership function, the clustering center set is indicated as S, the term S signifies the membership matrix, the term X_n indicates the cluster center, and M denotes the cluster dataset, respectively. The segmented result obtained based on BHEFC is represented as, D_g.

3.4 Feature Extraction Using CNN, GLCM Features, And Convolution-Based Local Directional Pattern

The segmented image D_g is given to the feature extraction step, which is carried out based on CNN features, GLCM features, and the proposed Convolution-based LDP toperform the extraction of features effectively. The feature extraction step performed in this research work is explained below,

a) CNN features: CNN is a multi-layered network utilized to detect complex features with special architecture from the segmented image output. This feature is said to be an AlexNet features. The CNN comprises three different layers, namely the pooling layer, the convolution layer, and the fully connected layer. Here, the first layer is the convolution layer, which extracts the essential features from the segmented image. It preserves the relations between the pixel values and image features. It takes the segmented result D_g as input and CNN features are extracted using the convolution layer. The features at the first convolution layer are extracted and are termed CNN features and are represented f_1 with dimension $\left[1\times 256\right]$, respectively. Fig. 2 depicts the extracted CNN feature based on the convolution layer.

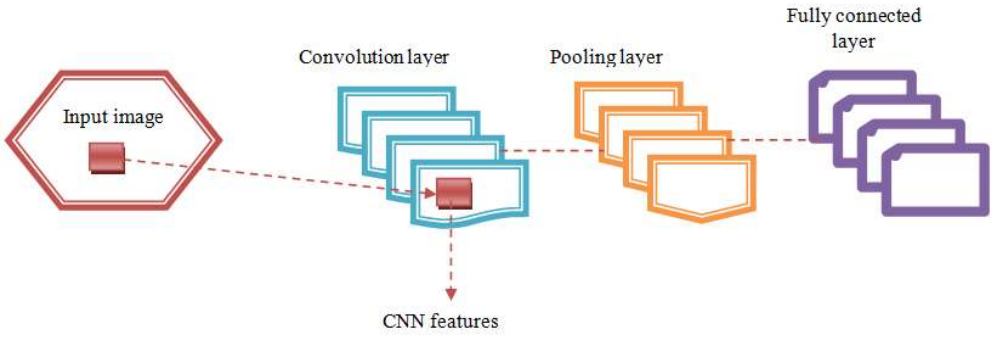

Fig. 2. *CNN feature extraction*

The CNN feature is represented as f_1.

b) GLCM features: GLCM [19] is utilized for extracting image features by mapping gray-level cooccurrence probabilities in various angular directions using spatial relations of pixels. In addition, the frequency is computed for reappearing the gray level image at different locations in the image. The correlation, energy, contrast, and homogeneity are the features extracted using GLCM, and the explanation is described below.

Correlation: It returns the measure of how the pixel is correlated to its neighboring pixel in the image. The correlation value ranges from -1 to 1. The three conditions for correlation are as follows: a) When correlation=one the positive relation, b) If the correlation=zero, no relation between the pixel of the image, and c) When the correlation is -1 , then it is said to be a negative relation.

Contrast: It is utilized to measure the intensity contrast between the pixel and neighbor over inter image. Here, the contrast should be zero for a constant image, and the expression for contrast is given below.

$$C = \sum_{uv} |u-v|^2 p(u,v) \tag{7}$$

where the pixel and their neighbor are denoted as u and v.

Energy: It is used to sum the square elements in the GLCM, and the range is between 0 and 1. For the constant image, the energy is said to be one, and the expression is given by,

$$E = \sum_{uv} p(u,v) \tag{8}$$

Homogeneity: It measures the closeness of elements distribution in GLCM to GLCM diagonal. The diagonal homogeneity is considered when the homogeneity is equal to one, and the equation is expressed as,

$$J = \sum_{uv} \frac{p(u,v)}{1+|u-v|} \tag{9}$$

The GLCM feature is denoted as f_2.

c) Convolution-based Local Directional Pattern

This sub-section presents the proposed convolution-based LDP for feature extraction. Fig. 3 depicts the extracted Convolutional-based LDP. LDP is considered an enhanced local pattern descriptor, in which the convolution operation is performed in the image. Here, the LDP is in binary format, which means zeros and ones. Initially, the input image and the convolution-based LDP form image are combined resulting in replacing pixel with convolution result. After that, the converted LDP input image and the convolution result image are averaged to get the final pixel value, and the expression of the final pixel value is given as,

$$Y_3 = \frac{Y_1 + Y_2}{2} \tag{10}$$

The convolution-based LDP feature is expressed as f_3 .Finally, the feature vector obtained from the feature extraction step is expressed as,

$$F = \{ f_i ; 1 < 1 < n \} \tag{11}$$

3.5 Skin Disease Detection Using the Proposed Social Crow Search-Based Deep Recurrent Neural Network

Once the features are extracted, the skin disease detection is carried out using the proposed SCS-based Deep RNN. Here, the feature vector F is applied as the input to the Deep RNN. For effective classification of skin disease, the Deep RNN is used, and the weights-biases are determined using the proposed algorithm optimally. The architecture of Deep RNN and the algorithmic steps of the proposed SCS are described below.

3.5.1 Architecture of The Deep RNN

Deep RNN [2] is the network architecture that contains multiple recurrent hidden layers in the layer of the network hierarchy. In Deep RNN, the recurrent connection exists at the hidden layer. The Deep RNN classifier effectively operates under the varying input feature length based on the sequence of information. It uses the knowledge of the previous state as input in the current prediction and processes the iteration using the hidden state information. The recurrent feature makes the Deep RNN to be highly effective in working with the features. Due to the sequential pattern of information, Deep RNN is considered the best classifier among the traditional deep learning approaches. The architecture of Deep RNN is represented in Fig. 3.

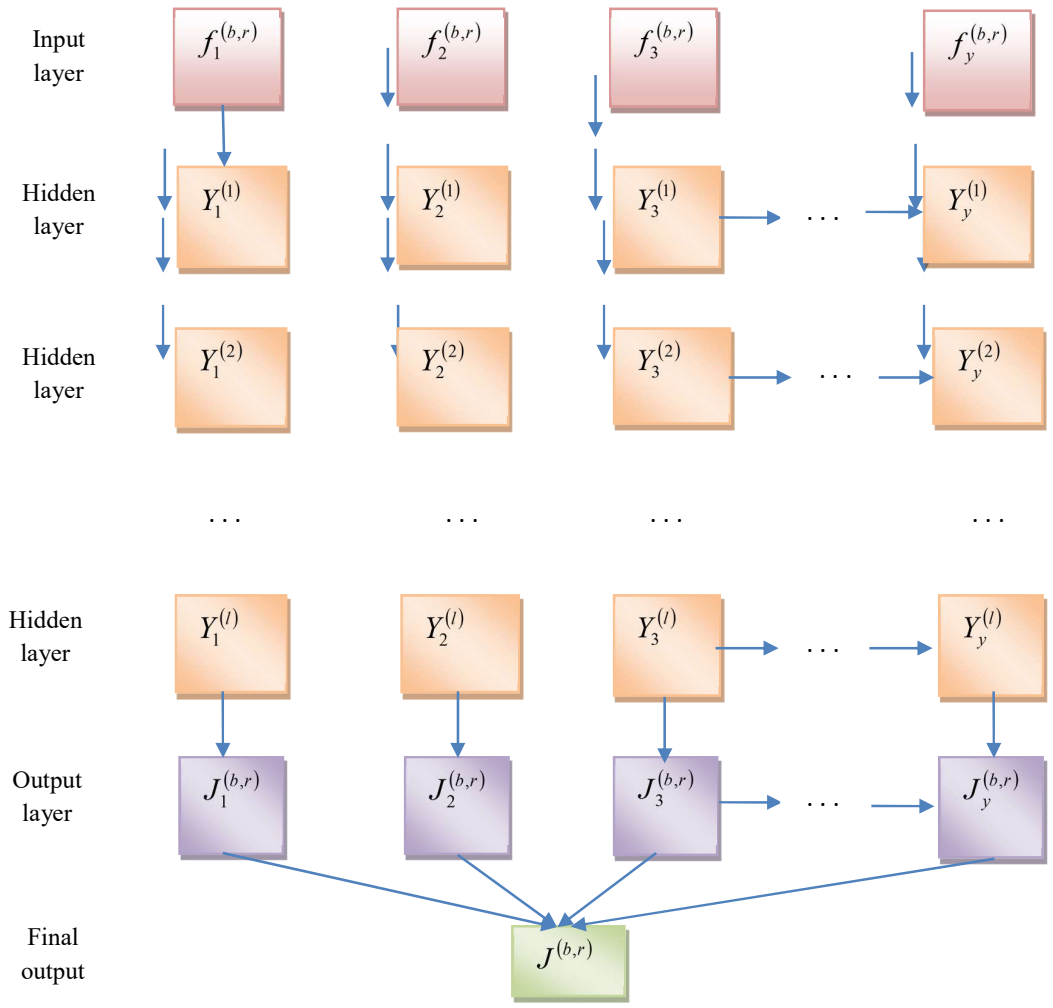

Fig. 3.*The architecture of the Deep RNN classifier*

The structure of Deep RNN is made by considering the input vector of b^{th} layer at r^{th} time as $F^{(b,r)}=\left\{f_1^{(b,r)},f_2^{(b,r)},\ldots f_i^{(b,r)},\ldots f_y^{(b,r)}\right\}$ and the output vector of b^{th} layer at r^{th} time as $J^{(b,r)}=\left\{J_1^{(b,r)},J_2^{(b,r)},\ldots J_i^{(b,r)},\ldots J_y^{(b,r)}\right\}$, respectively. The pair of each element of input and the output vectors is termed as the unit. Here, i denotes the arbitrary unit number of b^{th} layer, and y represents the total number of units of b^{th} layer.

In addition to this, the arbitrary unit number and the total number of units of $(b-1)^{th}$ layer are denoted as j and E, respectively. At this time, the input propagation weight from $(b-1)^{th}$ layer to b^{th} layer is represented as, $W^{(b)}\in H^{y\times E}$, and the recurrent weight of b^{th} layer is represented as $w^{(b)}\in H^{y\times y}$. Here, H denotes the set of weights. However, the components of the input vector is expressed as,

$$F_i^{(b,r)}=\sum_{z=1}^{E}p_{iz}^{(b)}J_z^{(b-1,r)}+\sum_{i'}^{y}x_{ii'}^{(b)}J_{i'}^{(b,r-1)} \tag{12}$$

where, $p_{iz}^{(b)}$ and $x_{ii'}^{(b)}$ are the elements of $W^{(b)}$ and $w^{(b)}$. i' denotes the arbitrary unit number of b^{th} layer. The elements of the output vector of b^{th} layer are represented as,

$$J_i^{(b,r)}=\beta^{(b)}\left(F_i^{(b,r)}\right) \tag{13}$$

where, $\beta^{(b)}$ denotes the activation function. However, the activation functions, like the sigmoid function $\beta(F)=\tanh(F)$, ReLU $\beta(F)=\max(F,0)$, and the logistic sigmoid function $\beta(F)=\frac{1}{\left(1+e^{-F}\right)}$ are the frequently used activation functions.

To simplify the process, 0^{th} weight as $p_{i0}^{(b)}$ and 0^{th} unit as $J_0^{(b-1,r)}$ are introduced, and hence the bias is represented as,

$$J^{(b,r)}=\beta^{(b)}.\left(W^{(b)}J^{(b-1,r)}+w^{(b)}.J^{(b,r-1)}\right) \tag{14}$$

Here, $J^{(b,r)}$ denotes the output of the classifier.

3.5.2 Algorithmic Steps of the Proposed Social Crow Search For Training Deep Recurrent Neural Network

The developed SCS for skin disease detection is illustrated in this section. The proposed SCS is the combination of CSA [16], and SSD [15] and thus attains the advantages of SSD in CSA. The SSD algorithm is inspired by various evolutionary optimization approaches to minimize the SVM parameters to enhance the system performance. The main aim of SSD is to search in the space for optimal or near-optimal solutions. This method is very efficient for generating improved features to tackle multi-objective optimization issues. Moreover, the method can solve highly non-linear problems with complex constraints. The standard CS, a population-dependent optimization, depends on the intelligent behavior of the crows in searching for their prey and locating the prey based on memory. The intelligence of the crow is exhibited in the mimicking behavior of the crows, which follow their neighbors in locating the position of the food. In addition, they possess the memory of the previous location of food. Thus, CSA exhibits the crows' behavior and the search mechanism of the crows is based on the adjustable parameters, like awareness probability and flight length. The adjustable parameters are tune able and they depend on the decision variables, constraints, and objective functions, and the main function of these adjustable parameters is that they control the intensification and diversification of CSA. Moreover, the algorithm exhibits a better trade-off between the diversification and the intensification phases effectively, and the convergence rate is very high highlighting the minimal computational time. The steps followed in the SCS are described below, and the procedure comprises two main conditions:

Condition 1: The e^{th} crow updates the position only when the random value corresponding to the c^{th} crow exceeds the awareness probability of the randomly chosen c^{th} crow.

Condition 2: In the second condition, the random selection of the solution is progressed based on the feasibility of the new position of the crow. In the case of the non-feasible solution and when the random value corresponding to c^{th} crow lies below the awareness probability of the c^{th} crow, the random selection of the solution is carried out.

a) Initialization: The first step in the proposed optimization algorithm is the solution initialization that initializes the population of the crow in the ∂ dimensional area. The solution in the ∂ dimensional area or search space is given as,

$$\begin{bmatrix} Z_1^1 & Z_2^1 & . & . & Z_\partial^1 \\ Z_1^2 & Z_2^2 & . & . & Z_\partial^2 \\ . & . & . & . & . \\ . & . & . & . & . \\ Z_1^a & Z_2^a & . & . & Z_\partial^a \end{bmatrix} \tag{15}$$

where, a is the total number of crows in the search space, and Z_∂^a is the position of the a^{th} crow in the dimensional area. Here, $Z\in H^{y\times E}, H^{y\times y}$ The memory of the crow is given as,

$$n=\begin{bmatrix} n_1^1 & n_2^1 & . & . & n_\partial^1 \\ n_1^2 & n_2^2 & . & . & n_\partial^2 \\ . & . & . & . & . \\ . & . & . & . & . \\ n_1^a & n_2^a & . & . & n_\partial^a \end{bmatrix} \tag{16}$$

where, n is the memory, which takes the matrix form, of the crow in the search space. In the initial iteration, the crows do not have any idea regarding the location of the hidden food. Hence, the hidden food is assumed to be in the initial position of the crow and the crow memorizes the location of the hidden food.

b) Evaluation of the objective function: The selection of the optimal position of the crow is performed based on the minimization problem. The minimal value of the objective function describes the better solution and therefore, the solution with the minimum value of the error is chosen as the best solution. The error is computed as,

$$L_n = \frac{1}{\sigma}\sum_{\nu=1}^{\sigma} J_{\nu}^{(b,r)} - \kappa_{\nu} \tag{17}$$

where L_n denotes the fitness value of n^{th} atom, $J_{\nu}^{(b,r)}$ denotes the output of the classifier, and κ_{ν} denotes the estimated output.

c) Location update using the proposed SCS algorithm: After computing the objective function, the solution undergoes the location update based on the SCS algorithm. Thus, the updated equation of CSA is expressed as,

$$Z_e(\tau+1) = Z_e(\tau) + k_1 * xy_e(\tau)\left[n_v(\tau) - Z_e(\tau)\right] \tag{18}$$

where $Z_e(\tau+1)$ refers to the position update of e^{th} crow in the next iteration, $Z_e(\tau)$ and indicates the position update of the e^{th} crow in the previous iteration. The random number and the flight length of e^{th} crow are denoted as, k_e and $xy_e(\tau)$, respectively. The memory of v^{th} crow is indicated as $n_v(\tau)$. Equation (9) specifies that the new position of the crow is based on the position and the flight length of the corresponding crow in the previous iteration, and the memory of the neighboring crow, and equation (11) is modified using the SSD to improve the effectiveness of the approach and to identify the solutions to several optimization problems. The updated equation of the SSD velocity $h_e(\tau)$ is given by,

$$Z_e(\tau+1) = Z_e(\tau) + h_e(\tau) \tag{19}$$

$$Z_e(\tau+1) = Z_e(\tau) + l\sin(k_1)\left(r_e(\tau) - Z_e(\tau)\right) + \sin(k_1)\left[n_v(\tau) - Z_e(\tau)\right]; if\ k_e \le 0.5 \tag{20}$$

$$Z_e(\tau+1) = Z_e(\tau) + l\sin(k_1) r_e(\tau) - l\sin(k_1) Z_e(\tau) + \sin(k_1) n_v(\tau) - \sin(k_1) Z_e(\tau) \tag{21}$$

$$n_v(\tau) = \frac{Z_e(\tau+1) - Z_e(\tau) - l\sin(k_1) r_e(\tau) + l\sin(k_1) Z_e(\tau) + \sin(k_1) Z_e(\tau)}{\sin(k_1)} \tag{22}$$

Assume $n_v(\tau) = \frac{Z_\beta + Z_\gamma + Z_\alpha}{3}$, then the equation (15) is rearranged as,

$$\frac{Z_\beta + Z_\gamma + Z_\alpha}{3} = \frac{Z_e(\tau+1) - Z_e(\tau) - l\sin(k_1) r_e(\tau) + l\sin(k_1) Z_e(\tau) + \sin(k_1) Z_e(\tau)}{\sin(k_1)} \tag{23}$$

$$Z_\beta + Z_\gamma + Z_\alpha = 3\left[\frac{Z_e(\tau+1) - Z_e(\tau) - l\sin(k_1) r_e(\tau) + l\sin(k_1) Z_e(\tau) + \sin(k_1) Z_e(\tau)}{\sin(k_1)}\right] \tag{24}$$

$$Z_\beta = 3\left[\frac{Z_e(\tau+1) - Z_e(\tau) - l\sin(k_1) r_e(\tau) + l\sin(k_1) Z_e(\tau) + \sin(k_1) Z_e(\tau)}{\sin(k_1)}\right] - Z_\gamma - Z_\alpha \tag{25}$$

where the term h_e denotes the velocity of Z_e, and the uniformly distributed random numbers are indicated as k_1 and k_2 ranging from 0 to 1. The term $r_e(\tau)$ represents the best solution of e^{th} agent, and the term n_v indicates the mean global solution for the whole population.

Substituting equation (18) in equation (11),

$$Z_e(\tau+1) = Z_e(\tau) + k_1 * xy_e(\tau)\left[\begin{array}{l} 3\left[\frac{Z_e(\tau+1) - Z_e(\tau) - l\sin(k_1) r_e(\tau) + l\sin(k_1) Z_e(\tau) + \sin(k_1) Z_e(\tau)}{\sin(k_1)}\right] - \\ Z_\gamma - Z_\alpha - Z_e(\tau) \end{array}\right] \tag{26}$$

$$Z_e(\tau+1) = Z_e(\tau) + k_1 * xy_e(\tau)\left[\frac{3}{\sin(k_1)} Z_e(\tau+1) + \frac{1}{\sin(k_1)}\left[3\left[\begin{array}{l} -Z_e(\tau) - l\sin(k_1) r_e(\tau) + l\sin(k_1) Z_e(\tau) \\ +\sin(k_1) Z_e(\tau) \end{array}\right] - \sin(k_1) Z_e(\tau)\right] - Z_\gamma - Z_\alpha\right] \tag{27}$$

$$Z_e(\tau+1) = Z_e(\tau) + k_1 xy_e(\tau)\frac{3}{\sin(k_1)} Z_e(\tau+1) + \frac{k_1 xy_e(\tau)}{\sin(k_1)}\left[\begin{array}{l} -3Z_e(\tau) - 3l\sin(k_1) r_e(\tau) + 3l\sin(k_1) Z_e(\tau) \\ +3\sin(k_1) Z_e(\tau) - \sin(k_1) Z_e(\tau) \end{array}\right] - k_1 xy_e(\tau)\left(Z_\gamma + Z_\alpha\right) \tag{28}$$

$$Z_e(\tau+1) - k_1 xy_e(\tau)\frac{3}{\sin(k_1)} Z_e(\tau+1) = Z_e(\tau) + \frac{k_1 xy_e(\tau)}{\sin(k_1)}\left[2\sin(k_1) Z_e(\tau) - 3Z_e(\tau) + 3l\sin(k_1)\left(Z_e(\tau) - r_e(\tau)\right)\right] - k_1 xy_e(\tau)\left(Z_\gamma + Z_\alpha\right) \tag{29}$$

$$Z_e(\tau+1)\left[1 - \frac{k_1 xy_e(\tau) 3}{\sin(k_1)}\right] = Z_e(\tau) + \frac{k_1 xy_e(\tau)}{\sin(k_1)}\left[2\sin(k_1) Z_e(\tau) - 3Z_e(\tau) + 3l\sin(k_1)\left(Z_e(\tau) - r_e(\tau)\right)\right] - k_1 xy_e(\tau)\left(Z_\gamma + Z_\alpha\right) \tag{30}$$

$$Z_e(\tau+1)\left[\frac{\sin(k_1)-k_1 xy_e(\tau)3}{\sin(k_1)}\right]=Z_e(\tau)+\frac{k_1 xy_e(\tau)}{\sin(k_1)}\left[2\sin(k_1)Z_e(\tau)-3Z_e(\tau)+3l\sin(k_1)(Z_e(\tau)-r_e(\tau))\right]-k_1 xy_e(\tau)(Z_\gamma+Z_\alpha) \quad (31)$$

$$Z_e(\tau+1)=\frac{\sin(k_1)}{\sin(k_1)-3k_1 xy_e(\tau)}\left[Z_e(\tau)+\frac{k_1 xy_e(\tau)}{\sin(k_1)}\left[2\sin(k_1)Z_e(\tau)-3Z_e(\tau)+3l\sin(k_1)(Z_e(\tau)-r_e(\tau))\right]-k_1 xy_e(\tau)(Z_\gamma+Z_\alpha)\right] \quad (32)$$

where, the terms r_1 and r_2 signifies the random number ranging from 0 and 1, the second and third best solution is represented as Z_γ and Z_α.

d) Compute the objective function for the newly generated position of the crows: The e^{th} crow updates the position only when the random value of the c^{th} crow is greater than or equal to the awareness probability of c^{th} crow at iteration t. If the random value lies below the awareness probability, the crow updates the position depending on the random search mechanism. The position of e^{th} crow is given as,

$$Z_e(\tau+1)=\begin{cases}\dfrac{[1-\kappa_1\times\hbar]}{(\kappa_e\times H_e(\tau))-(\kappa_1\times\hbar)}\begin{Bmatrix}\dfrac{\kappa_e\times H_e(\tau)}{[1-\kappa_1\times\hbar]}\left(\mu_e(\tau)+\kappa_1\times\hbar\times Z_{best}\right)+\\ \kappa_e\times H_e(\tau)\times r_c(\tau)-\dfrac{\mu_e(\tau)+\kappa_1\times\hbar\times Z_{best}}{[1-\kappa_1\times\hbar]}\end{Bmatrix} & ; \quad \kappa_c\geq DQ_c(\tau)\\ Random\ process & ; \quad Otherwise\end{cases} \quad (33)$$

where, $DQ_c(\tau)$ signifies awareness probability of c^{th} crow at iteration τ.

e) Crow updates the memory*:* After the crow finds the position of the hidden food, the fitness is evaluated, which should be a minimal value. The new position is used only when the fitness of the crow's position in the current iteration is better than the fitness of the crow in the previous iteration. The fitness of the solution is computed based on equation (10). Thus, the newly updated position is memorized such that the crow uses the memory to determine the position of the hidden food in the future. The memory update is given as,

$$r_e(\tau+1)=\begin{cases}Z_e(\tau+1) & ; \quad fit(Z_e(\tau+1))<fit(Z_e(\tau))\\ Z_e(\tau) & ; \quad Otherwise\end{cases} \quad (34)$$

f) Stopping criterion: The steps are repeated from step b) to e) until the global solution is determined and the optimal weights are derived using the proposed algorithm. The pseudo-code of the developed BHEFC+SCS-Deep RNN is depicted in Algorithm 1, which demonstrates a step-wise description of the algorithm.

Algorithm 1. Pseudocode for the proposed BHEFC+SCS-Deep RNN

```
Input: Crow Population
Output: Best solution
Procedure:
Begin
      Initialization of crow population
Calculate the Objective Function
    If (κc ≥ DQc(τ))
     {
      Updates the crow position based on equation (32)
      Else
      Update the position based on the Random search
      }
 Calculate the objective function of the new solution set
    If (fit(Ze(τ+1)) < fit(Ze(τ)))
     {
      Update the Memory of the crow
Else
      Remain in the initial position, Ze(τ)
      }
   End
```

4. Results and Discussion

The results of the proposed BHEFC+SCS-Deep RNN are discussed in this section based on the evaluation metrics.

4.1 Experimental Arrangement

The experimentation of the BHEFC+SCS-Deep RNN is performed on Windows 10 OS with 2GB RAM and an Intel i3 core processor. The implementation of the proposed method was done using Python.

4.2 Dataset Description

The experimentation is done using a Skin cancer dataset [17], and the description of the dataset is given below:

Skin cancer Dataset: In this dataset, dermatoscopic images are collected from various populations acquired and stored by different modalities. Moreover, the skin disease dataset contains 34 attributes, out of which, 33 attributes are linear, and the remaining attribute is nominal. Here, all the datasets are deposited in Harvard Data verse.

4.3 Evaluation Metrics

The performance of the proposed BHEFC+SCS-Deep RNN is employed for analyzing the methods using accuracy, sensitivity, and specificity, and they are formulated below,

a) Accuracy: It is the measure of accurate positive classified results to the total number of measures, and is expressed as,

$$Accuracy = \frac{X + Y}{X + P + Y + O} \tag{35}$$

where Y refer to the true positives, and the true negative is indicated as X. The term O signifies the false positives and P be the false negatives.

b) Sensitivity: Sensitivity defines the measure of positiveness and is computed using the below expression.

$$Sensitivity = \frac{Y}{P + Y} \tag{36}$$

c) Specificity: Specificity is otherwise as TNR, which is the measure of false negatives. Specificity is represented as,

$$Specificity = \frac{X}{X + O} \tag{37}$$

d) TPR: The expression for TPR is given below,

$$TPR = 1 - Sensitivity \tag{38}$$

4.4 Experimental Results

The experimental results obtained by the proposed model are given in this section. Fig. 4 depicts the sample results of skin disease detection. Fig. 4(a), 4(b), and 4(c) show the input image-1, 2, and 3, and fig. 4(d), 4(e), and 4(f) depicts the segmented output of image-1, image-2, and image-3 using BHEFC. Fig. 4(g), 4(h), and 4(i) illustrates the LDP feature output for image-1, image-2, and image-3, and fig. 4(j), 4(k), and 4(l) shows the histogram output of image-1, image-2, and image-3.

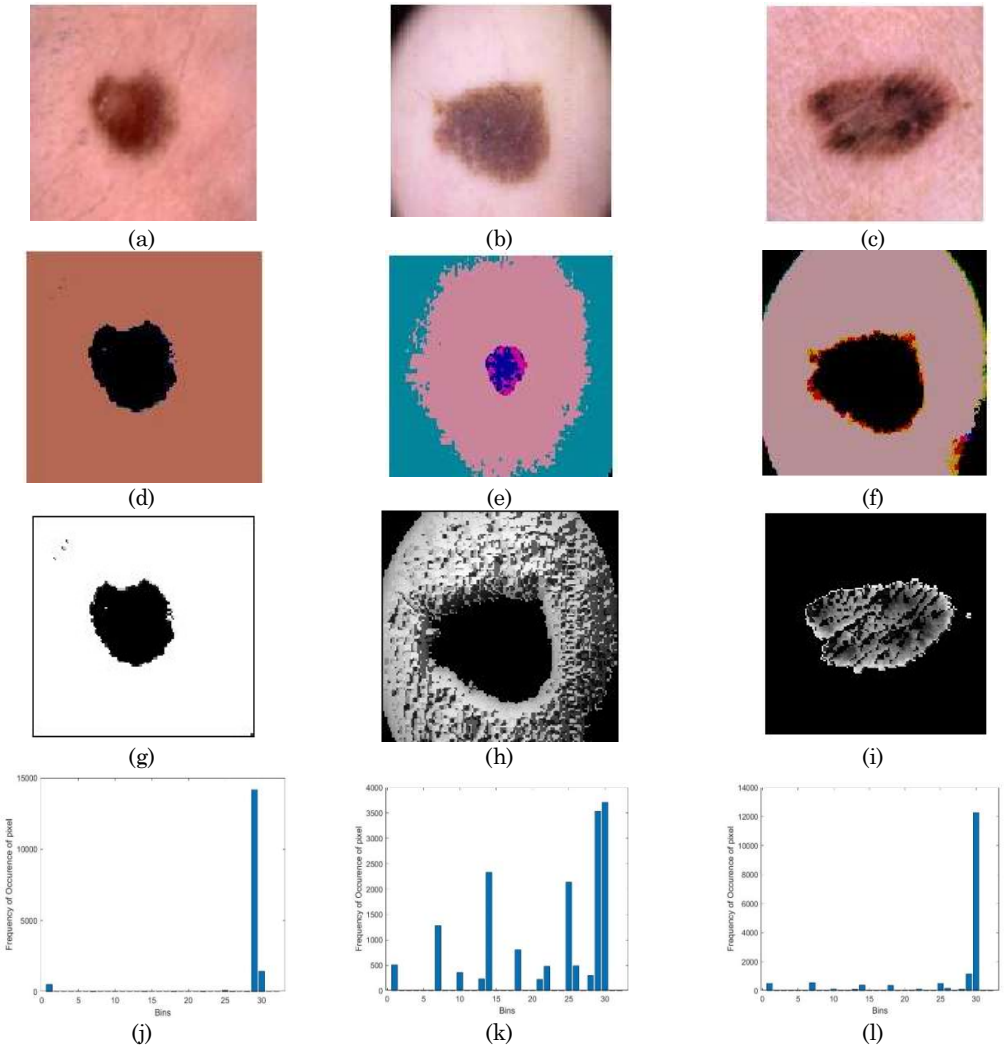

Fig. 4 *Sample results *a) Input image-1, (b) Input image-2, (c) Input image-3, (d) Segmented output of image-1, (e) Image-2 segmented output, (f) Segmented output of image-3, (g) LDP feature output of image-1, (h) Image-2 LDP feature output, (i) LDP feature output of image-3, (j) Histogram output of image-1, (k) Histogram output of image-2, (l) Histogram output of image-3*

4.5 Performance Analysis

The performance analysis made using the proposed BHEFC+SCS-Deep RNN by varying the training percentage and K-Fold is discussed below:

a) Performance analysis with training percentage

Fig. 5 portrays the performance analysis of the proposed detection mechanism with different hidden neurons. Fig. 5(a) shows the performance analysis of accuracy to training percentage. When training percentage=40%, the accuracy obtained by the proposed BHEFC+SCS-Deep RNN with hidden neurons 100 is 89.80%, hidden neurons 200 is 89.99%, hidden neurons 300 is 90.18%, hidden neurons 400 is 90.37%, and hidden neurons 500 is 90.55%, respectively. When training percentage=90%, the accuracy obtained by the proposed model with hidden neurons 100 is 92.12%, hidden neurons 200 is 92.32%, hidden neurons 300 is 92.51%, hidden neurons 400 is 92.69%, and hidden neurons 500 is 92.86% respectively.

Fig. 5(b) shows the performance analysis of sensitivity to training percentage. When training percentage=40%, the sensitivity obtained by the proposed model with hidden neurons 100 is 89.82%, hidden neurons 200 is 90.01%, hidden neurons 300 is 90.19%, hidden neurons 400 is 90.38%, and hidden neurons 500 is 90.56%, respectively. When training percentage=90%, the sensitivity obtained by the proposed model with hidden neurons 100 is 92.14%, hidden neurons 200 is 92.33%, hidden neurons 300 is 92.52%, hidden neurons 400 is 92.71%, and hidden neurons 500 is 92.88% respectively.

Fig. 5(c) shows the performance analysis of specificity to training percentage. When training percentage=40%, the specificity obtained by the proposed model with hidden neurons 100 is 89.72%, hidden

neurons 200 is 89.93%, hidden neurons 300 is 90.09%, hidden neurons 400 is 90.30%, and hidden neurons 500 is 90.46%, respectively. When training percentage=90%, the specificity obtained by the proposed model with hidden neurons 100 is 92.02%, hidden neurons 200 is 92.23%, hidden neurons 300 is 92.44%, hidden neurons 400 is 92.60%, and hidden neurons 500 is 92.74% respectively.

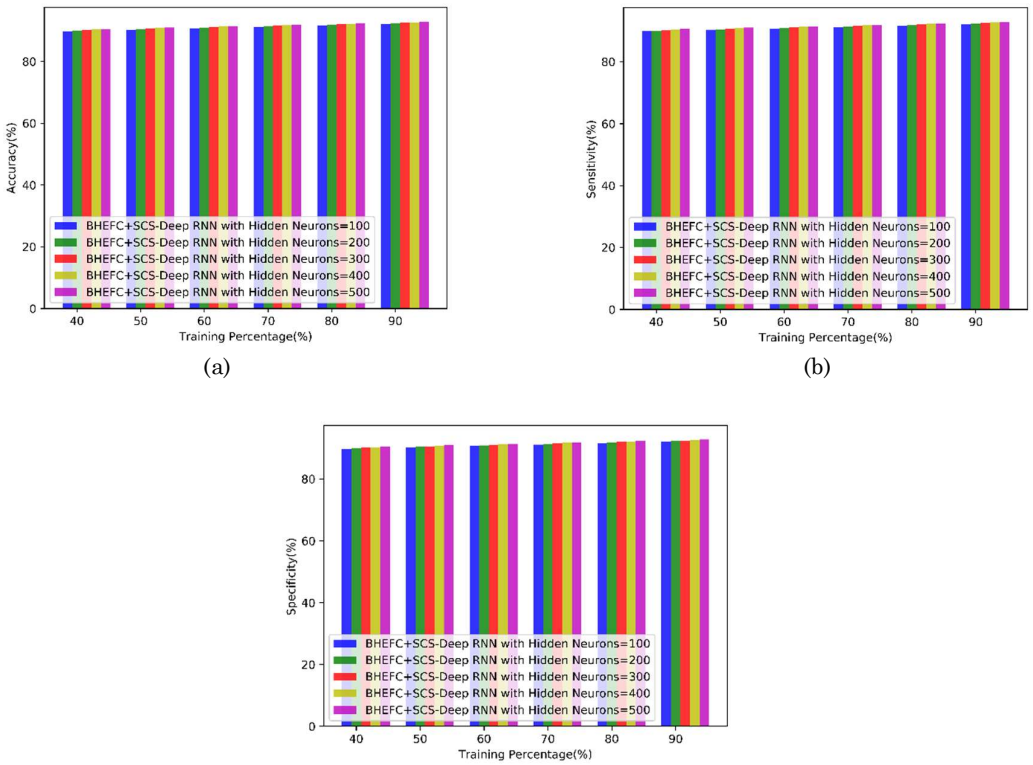

Fig. 5. *Performance analysis, (a) accuracy (b) sensitivity, and (c) specificity,*

b) Performance analysis based on K-Fold

Fig. 6 portrays the performance analysis of the proposed detection mechanism with different hidden layers. Fig. 6(a) shows the performance analysis of accuracy to K-Fold. When K-Fold=5, the accuracy obtained by the proposed BHEFC+SCS-Deep RNN with hidden neurons 100 is 88.89%, hidden neurons 200 is 89.07%, hidden neurons 300 is 89.26%, hidden neurons 400 is 89.44%, and hidden neurons 500 is 89.63%, respectively. When K-Fold=10, the accuracy obtained by the proposed model with hidden neurons 100 is 91.19%, hidden neurons 200 is 91.37%, hidden neurons 300 is 91.56%, hidden neurons 400 is 91.75%, and hidden neurons 500 is 91.93% respectively.

Fig. 6(b) shows the performance analysis of sensitivity to K-Fold. When K-Fold=6, the sensitivity obtained by the proposed model with hidden neurons 100 is 89.36%, hidden neurons 200 is 89.55%, hidden neurons 300 is 89.73%, hidden neurons 400 is 89.92%, and hidden neurons 500 is 90.10%, respectively. When K-Fold=9, the sensitivity obtained by the proposed model with hidden neurons 100 is 90.75%, hidden neurons 200 is 90.93%, hidden neurons 300 is 91.11%, hidden neurons 400 is 91.30%, and hidden neurons 500 is 91.48%, respectively.

Fig. 6(c) shows the performance analysis of specificity to K-Fold. When K-Fold=5, the specificity obtained by the proposed model with hidden neurons 100 is 88.81%, hidden neurons 200 is 89%, hidden neurons 300 is 89.18%, hidden neurons 400 is 89.36%, and hidden neurons 500 is 89.56%, respectively. When K-Fold=10, the specificity obtained by the proposed model with hidden neurons 100 is 91.10%, hidden neurons 200 is 91.25%, hidden neurons 300 is 91.48%, hidden neurons 400 is 91.67%, and hidden neurons 500 is 91.86%, respectively. The analysis based on comparative methods in terms of TPR metric is depicted in Fig. 7(d). Here, for the 80% FPR, the proposed model with hidden neurons 100, 200, 300, 400, and 500 have the TPR values of 89.45%, 89.63%, 89.80%, 90%, and 90.18% respectively.

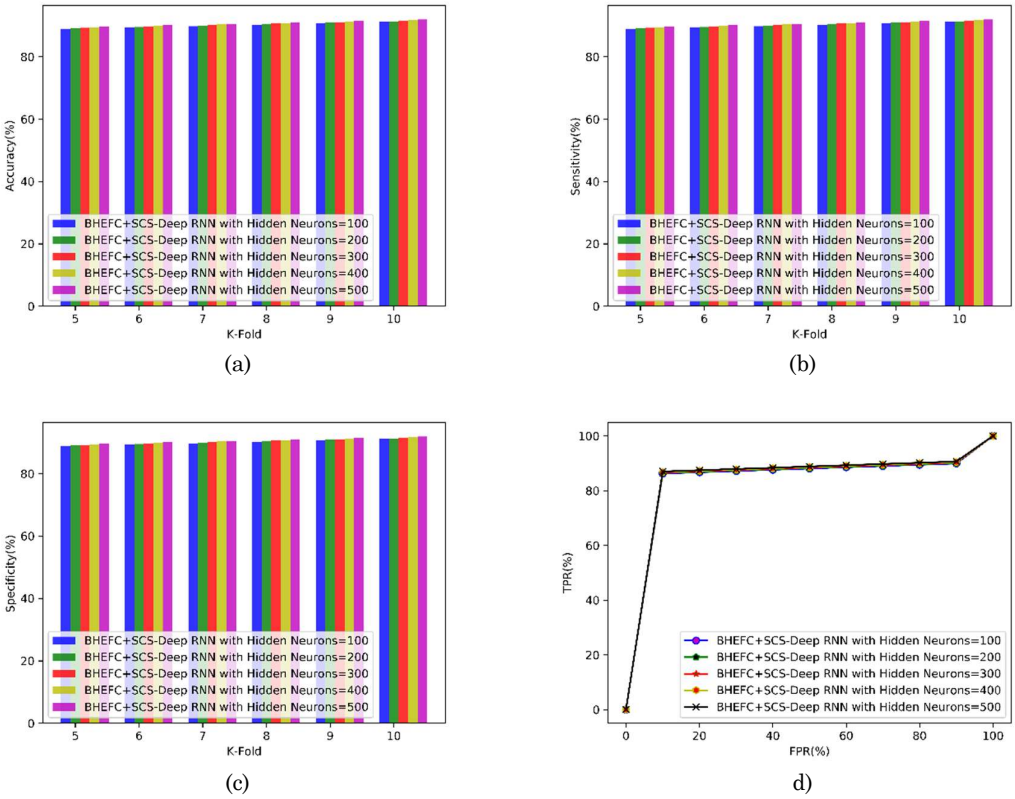

Fig. 6. *Performance analysis, (a) accuracy, (b) sensitivity, (c) specificity, and (d) TPR*

4.6 Comparative Techniques

Methods like Particle Swarm Optimization + Support Vector Machine (PSO+SVM) [8], BHEFC+ Bayesian classifier [1], PSO+RF, and BHEFC+ Deep RNN are utilized for the comparison with the developed BHEFC+SCS-Deep RNN for the analysis. The features considered for the comparative methods are as follows: The PSO+SVM and BHEFC+ Deep RNN methods consider each of the AlexNet feature and the statistical feature, whereas the statistical and Conv-LDP feature is considered by the BHEFC+ Bayesian classifier and PSO+RF. The developed model uses statistical, AlexNet, and the Con LDP feature.

4.6.1 Analysis of Skin Disease Detection to Training Data Percentage

The comparative analysis is analyzed in terms of accuracy, sensitivity, specificity, and TPR for skin disease detection is depicted in Fig. 7. Fig. 7a) illustrates the analysis using accuracy metrics with different training data percentages. When the training data percentage is 40, then the accuracy values computed by the existing PSO+SVM, BHEFC+Bayesian classifier, PSO+RF, BHEFC+Deep RNN, and proposed BHEFC+SCS-Deep RNN are 74.11%, 84.27%, 87.42%, 88.38%, and 88.83%, respectively. For 90% of training data, the existing techniques, like PSO+SVM is 78.12%, BHEFC+Bayesian classifier is 86.60%, PSO+RF is 92.13%, BHEFC+Deep RNN is 93.08%, and proposed BHEFC+SCS-Deep RNN is 93.54%, respectively.

The comparative analysis based on sensitivity is shown in Fig. 7(b). When the training data percentage is 50, the sensitivity values achieved by PSO+SVM, BHEFC+Bayesian classifier, PSO+RF, BHEFC+Deep RNN, and proposed BHEFC+SCS-Deep RNN are 82.41%, 88.39%, 88.64%, 89.33%, and 89.80%, respectively. For 90% of training data, the existing techniques, PSO+SVM, BHEFC+Bayesian classifier, PSO+RF, BHEFC+Deep RNN, and proposed BHEFC+SCS-Deep RNN, possess the sensitivity of 85.48%, 91.84%, 92.15%, 93.09%, and 93.56%, respectively.

The analysis in terms of specificity is shown in Fig. 7(c). When the training data percentage is 40, the specificity values achieved by PSO+SVM, BHEFC+Bayesian classifier, PSO+RF, BHEFC+Deep RNN, and proposed BHEFC+SCS-Deep RNN are 65%, 65%, 87.30%, 88.33%, and 88.75%, respectively. For 90% of training data, the existing techniques, PSO+SVM, BHEFC+Bayesian classifier, PSO+RF, BHEFC+Deep RNN, and proposed BHEFC+SCS-Deep RNN, possess the specificity of 65%, 68.69%, 92.04%, 93.03%, and 93.45%, respectively.

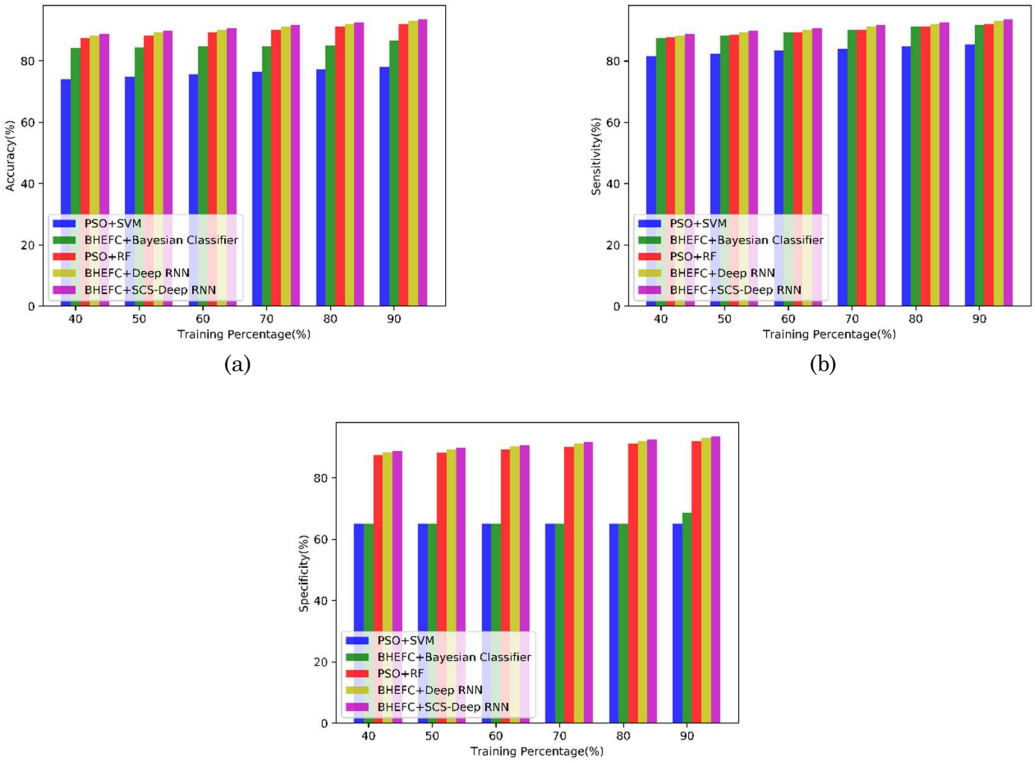

Fig. 7. *Comparative analysis by varying the training data percentages for skin disease detection (a) Accuracy, (b) Sensitivity, and (c) Specificity*

4.6.2 Analysis of the Skin Disease Detection To K-Fold

The comparative analysis is analyzed in terms of accuracy, sensitivity, specificity, and TPR for skin disease detection is depicted in Fig. 8. Fig. 8a) illustrates the analysis using accuracy metrics with different K-Fold. When K-Fold =5, then the accuracy values computed by existing PSO+SVM, BHEFC+Bayesian classifier, PSO+RF, BHEFC+Deep RNN and proposed BHEFC+SCS-Deep RNN are 73.73%, 84.51%, 86.99%, 87.93%, and 88.39%, respectively. When K-Fold=10, the existing techniques, like PSO+SVM is 77.72%, BHEFC+Bayesian classifier is 87.33%, PSO+RF is 91.66%, BHEFC+Deep RNN is 92.61%, and proposed BHEFC+SCS-Deep RNN is 93.07%, respectively.

The comparative analysis based on sensitivity is shown in Fig. 8(b). When K-Fold= 6, the sensitivity values achieved by PSO+SVM, BHEFC+Bayesian classifier, PSO+RF, BHEFC+Deep RNN and proposed BHEFC+SCS-Deep RNN are 82.06%, 87.94%, 88.27%, 88.87%, and 89.34%, respectively. When K-Fold=10, the existing techniques, PSO+SVM, BHEFC+Bayesian classifier, PSO+RF, BHEFC+Deep RNN and proposed BHEFC+SCS-Deep RNN, possesses the sensitivity of 85.58%, 91.68%, 91.86%, 92.62%, and 93.08%, respectively.

The analysis in terms of specificity is shown in Fig. 8(c). When K-Fold= 5, the specificity values achieved by PSO+SVM, BHEFC+Bayesian classifier, PSO+RF, BHEFC+Deep RNN and proposed BHEFC+SCS-Deep RNN are 65%, 65%, 86.89%, 87.89%, and 88.32%, respectively. When K-Fold=10, the existing techniques, PSO+SVM, BHEFC+Bayesian classifier, PSO+RF, BHEFC+Deep RNN and proposed BHEFC+SCS-Deep RNN, possesses the specificity of 65%, 68.09%, 91.56%, 92.56%, and 92.98%, respectively. The analysis based on comparative methods in terms of TPR metric is depicted in Fig. 9(d). Here, for the 80% FPR, the methods, PSO+SVM, BHEFC+Bayesian classifier, PSO+RF, BHEFC+Deep RNN, and proposed BHEFC+SCS-Deep RNN have the TPR values of 83.56%, 89.40%, 89.63%, 90.33%, and 90.79%, respectively.

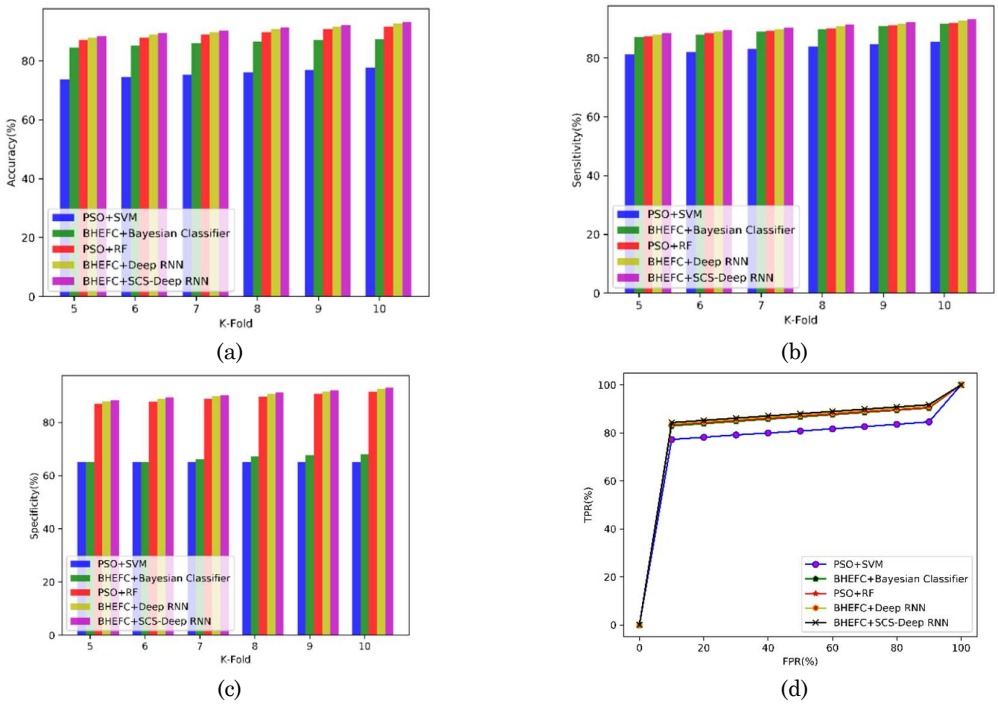

Fig. 8. *Comparative analysis by varying the K-Fold for skin disease detection (a) Accuracy, (b) Sensitivity, (c) Specificity, and (d) TPR*

4.7 Comparative Discussion

Table 1 depicts the comparative discussion of existing PSO+SVM, BHEFC+Bayesian classifier, PSO+RF, and BHEFC+Deep RNN, and the developed BHEFC+SCS-Deep RNN in terms of accuracy, sensitivity, and specificity parameters to training data percentages and K-Fold for skin disease detection. The maximum performance measured by the proposed BHEFC+SCS-Deep RNN in terms of accuracy parameter is 93.54%, whereas the accuracy values of existing PSO+SVM, BHEFC+Bayesian classifier, PSO+RF, and BHEFC+Deep RNN are 78.12%, 86.60%, 92.13%, and 93.08% respectively. The maximal sensitivity achieved by the proposed BHEFC+SCS-Deep RNN with the value of 93.56%, whereas the existing PSO+SVM, BHEFC+Bayesian classifier, PSO+RF, and BHEFC+Deep RNN acquired the sensitivity of 85.84%, 91.84%, 92.15%, and 93.09% respectively. The specificity value computed by proposed BHEFC+SCS-Deep RNN is 93.45%, whereas the existing PSO+SVM, BHEFC+Bayesian classifier, PSO+RF, and BHEFC+Deep RNN methods acquired the specificity of 65%, 68.69%, 92.04%, and 93.03% respectively

Table 1. *Comparative Discussion*

Metrics/Methods		PSO+SVM	BHEFC+Bayesian classifier	PSO+RF	BHEFC+Deep RNN	Proposed BHEFC+SCS-Deep RNN
Based on training data percentage	***Accuracy (%)***	78.12	86.60	92.13	93.08	**93.54**
	Sensitivity (%)	85.84	91.84	92.15	93.09	**93.56**
	Specificity (%)	65	68.69	92.04	93.03	**93.45**
Based on K-Fold	***Accuracy (%)***	77.72	87.33	91.66	92.61	**93.07**
	Sensitivity (%)	85.58	91.68	91.86	92.62	**93.08**
	Specificity (%)	65	68.09	91.56	92.56	**92.98**

5. Conclusion

This paper proposes a novel automated Deep RNN for skin disease detection. The proposed SCS is employed for training the Deep RNN. The proposed SCS is designed by combining CSA with the SSD algorithm, which can be utilized for finding the optimal weights to establish effective skin disease detection. The input image is initially given to the pre-processing step, which enhances the contrast of the image by removing the redundancies and noise in the original image. The segmentation module processes the image and transforms it into a segment using BHEFC. Here, the segmentation is performed on each input skin image using BHEFC. In addition, the feature extraction is performed using GLCM, CNN, and

the convolution-based LDP features for effective skin disease detection. Finally, skin disease detection is performed using SCS-based Deep RNN. The proposed BHEFC+SCS-Deep RNNoutperformed other methods with maximal accuracy of 93.54%, maximal sensitivity of 93.56%, and maximal specificity of 93.45%, respectively. In the future, other skin cancer datasets will be employed for computing the efficiency of the proposed method. In addition, advanced optimization techniques will be explored to further compute the efficiency of existing methods.

Compliance with Ethical Standards

Conflicts of Interest: Authors declared that they have no conflict of interest.

Human Participants: The conducted research follows the ethical standards and the authors ensured that they have not conducted any studies with human participants or animals.

References

[1] N. Noroozi, and A. Zakerolhosseini, "Differential diagnosis of squamous cell carcinoma in situ using skin histopathological images", Computers in biology and medicine, vol. 70, pp.23-39, 2016.
[2] J. Olsen, L. Themstrup, N. De Carvalho, M. Mogensen, G. Pellacani, and G.B.E. Jemec, "Diagnostic accuracy of optical coherence tomography in actinic keratosis and basal cell carcinoma", Photodiagnosis and photodynamic therapy, vol. 16, pp.44-49, 2016.
[3] V. R. Allugunti, "A machine learning model for skin disease classification using convolution neural network. International Journal of Computing", Programming and Database Management, Vol. 3(1), pp.141-147, 2022.
[4] P. Sakthivel, D.V.K. Irugu, A. Kakkar, K. Kaur, S. Jain, R. Pramanik, and A. Biswas, "Squamous cell carcinoma as a somatic-type malignancy in an extragonadal immature teratoma of the sinonasal region", International journal of pediatric otorhinolaryngology, vol. 126, p.109639, 2019.
[5] M. Wei, Q. Wu, H. Ji, J. Wang, T. Lyu, J. Liu, and L. Zhao, "A Skin Disease Classification Model Based on DenseNet and ConvNeXt Fusion", Electronics, Vol. 12(2), pp.438, 2023.
[6] V. K. Roy, V. Thakur, and N. Goyal, "Vision Transformer Framework Approach For Melanoma Skin Disease Identification", 2023.
[7] F. Joly, S. Deret, B. Gamboa, C. Menigot, P. Fogel, C. Mounier, P. Reiniche, F. Sidou, J. Aubert, J. Lear, and A. A. Fryer, "Photodynamic therapy corrects abnormal cancer-associated gene expression observed in actinic keratosis lesions and induces a remodeling effect in photodamaged skin", Journal of dermatological science, vol. 91, no. 2, pp.206-218, 2018.
[8] I. Abd El-Fattah, A. M. Ali, W. El-Shafai, T. E. Taha, and F. E. Abd El-Samie, "Deep-learning-based super-resolution and classification framework for skin disease detection applications", Optical and Quantum Electronics, Vol. 55(5), pp.427, 2023.
[9] Kempf, W., Mertz, K.D., Hofbauer, G.F. and Tinguely, M., "Skin cancer in organ transplant recipients", Pathobiology, vol. 80, no. 6, pp.302-309, 2013.
[10] B. Berman, and C. J. Cockerell, "Pathobiology of actinic keratosis: ultraviolet-dependent keratinocyte proliferation", Journal of the American Academy of Dermatology, vol. 68, no. 1, pp.S10-S19, 2013.
[11] J. M. Dodson, J. DeSpain, J. E. Hewett, and D. P. Clark, "Malignant potential of actinic keratoses and the controversy over treatment: a patient-oriented perspective", Archives of dermatology, vol. 127, no. 7, pp.1029-1031, 1991.
[12] C. Zheng, S. Qing, J. Wang, G. Lü, H. Li, X. Lü, C. Ma, J. Tang, and X. Yue, "Diagnosis of cervical squamous cell carcinoma and cervical adenocarcinoma based on Raman spectroscopy and support vector machine", Photodiagnosis and photodynamic therapy, vol. 27, pp.156-161, 2019.
[13] M. A. L. M. Boone, A. Marneffe, M. Suppa, M. Miyamoto, I. Alarcon, R. Hofmann-Wellenhof, J. Malvehy, G. Pellacani, and V. Del Marmol, "High-definition optical coherence tomography algorithm for the discrimination of actinic keratosis from normal skin and from squamous cell carcinoma", Journal of the European Academy of Dermatology and Venereology, vol. 29, no. 8, pp. 1606-1615, 2015.
[14] S. Schuh, R. Kaestle, E. C. Sattler, and J. Welzel, "Optical coherence tomography of actinic keratoses and basal cell carcinomas–differentiation by quantification of signal intensity and layer thickness", Journal of the European Academy of Dermatology and Venereology, vol. 30, no. 8, pp.1321-1326, 2016.
[15] A. Tharwat, and T. Gabel, "Parameters optimization of support vector machines for imbalanced data using social ski driver algorithm", Neural Computing and Applications, pp.1-14.
[16] A. Askarzadeh, "A novel metaheuristic method for solving constrained engineering optimization problems: crow search algorithm", Computers & Structures, vol. 169, pp.1-12, 2016.
[17] Skin disease dataset, "https://challenge2019.isic-archive.com/data.html", accessed in November 2019.
[18] J. Liu, F.-L. Chung, and S. Wang, "Black Hole Entropic Fuzzy Clustering", IEEE Transactions on Systems, Man, and Cybernetics: Systems, vol.48, no.9, pp.1622-1636, 2017.
[19] Md. Al-Amin, M. Badrul Alam, and Md. R. Mia, "Detection of Cancerous and Non-cancerous Skin by using GLCM Matrix and Neural Network Classifier", International Journal of Computer Applications, vol.132, no.8, pp.0975 – 8887, December2015.